Deuterium loading of redeposited-like W coatings present in tokamaks by ion implantation

R. Mateus [a,b,*], D. Dellasega [c,d], M. Passoni [c,d], Z. Siketić [e], I. Bogdanović Radović [e], J. Likonen [f], A. Hakola [f], E. Alves [a,b]

[a] *IPFN, Instituto Superior Técnico, Universidade de Lisboa, 2695-066, Bobadela, Portugal*
[b] *DECN, Instituto Superior Técnico, Universidade de Lisboa, 2695-066, Bobadela, Portugal*
[c] *Dipartimento di Energia, Politecnico di Milano, via Ponzio 34/3, 20133, Milano, Italy*
[d] *IFP, CNR, via R. Cozzi 53, Milano, 20125, Italy*
[e] *Ruđer Bošković Institute, P.O. Box 180, 10002, Zagreb, Croatia*
[f] *VTT Technical Research Centre of Finland Ltd., P.O. Box 1000, 02044, VTT, Finland*

ARTICLE INFO

ABSTRACT

Pulsed Laser deposition (PLD) is a suitable technique to reproduce W, W–O and W–N–O coatings resembling those present in tokamaks walls, as protective W coatings covering plasma facing components (PFCs) or W-based layers redeposited in PFCs during reactor operation. Nevertheless, difficulties still exist to codeposit deuterium in all such layers, and parallel methods need to be implemented to load it. W-based coatings with porous and columnar microstructures grown by PLD where loaded with flat depth contents of deuterium down to 0.4–0.6 μm using multiple ion implantation steps at distinct incident energies and fluences. Deuterium amounts close to 7 at. % were easily achieved. Similar deuterium contents are commonly observed in deposits in now-a-days tokamaks. Microstructural characterization of the coatings was carried out by scanning electron microscopy (SEM). Quantitative elemental analysis of as-deposited and as-implanted materials was accessed by elastic backscattering spectroscopy (EBS), nuclear reaction analysis (NRA) and by time-of-flight elastic recoil detection (ToF-ERDA). Secondary ion mass spectrometry (SIMS) revealed the depth profiles of the existing isotopes and, particularly, of retained deuterium. Beyond their use in ex-situ experiments, the production is useful to calibrate laser induced breakdown spectroscopy (LIBS) and SIMS setups, aiming a standard free depth-quantification of deuterium in W-based coatings.

1. Introduction

Tungsten (W) was selected as the main material to cover the walls of nuclear fusion reactors due to its distinct properties such as low neutron activation, low hydrogen retention, high thermal conductivity enhancing heat exhaust during transient heat loads, high melting point and low erosion rates caused by physical sputtering [1]. However, during the extended operations of fusion reactors, erosion of the W walls is unavoidable, which leads to the transport of W particles and to their co-deposition with other elemental impurities on the reactor walls [2]. The deposits commonly consist of hydrogen isotopes and helium (He), the main components of the plasma gas and exhaust, as well as oxygen (O), a natural contaminant, or even nitrogen (N), argon, neon or krypton, injected in the divertor zone as seeding gas in plasma-seeding experiments [2]. Examples of W deposits found in exposed plasma facing components (PFCs) are those observed at the full W wall of ASDEX Upgrade after irradiation under high (tens of eV) [3] and low (close to 1 eV) [4] plasma energies, promoting the growth of amorphous and porous W microstructures (a-W and p-W, respectively). Similar and more complex deposits were recently observed in the WEST tokamak [5, 6] A third microstructure is also observed in tokamaks. W coatings with a columnar structure (c-W) are produced to cover part of the full-W walls of ASDEX Upgrade and other reactors [7]. Different structures and elemental compositions result in distinct behaviours of PFCs under irradiation. To investigate this issue, coatings with W structures mimicking those observed in present-day tokamaks are produced and exposed to relevant irradiation conditions in ex-situ or in-situ experiments to predict their life-times. In this regard, the pulsed laser

---

deposition (PLD) method proved to be a successful technique to reproduce all these structures (a-W, p-W, c-W) and codeposited compositions expected in present-day tokamaks [8,9]. Different coatings of W, W–O and W–N–O grown by PLD were used for experiments in tokamaks, linear plasma devices and ion beams facilities to investigate morphological modifications [8–15] as well retention of light elements imposed by irradiation with plasma and ion beams, i.e., ^{1}H, ^{2}H and O [10–15].

Previous attempts to grow W-based coatings by PLD with significant codeposited amounts of deuterium (^{2}H) were performed to reproduce some of the deposits. In that case, ^{2}H was introduced in the deposition atmosphere. However, the maximum incorporated ^{2}H amounts were of the order of ~0.3 at.%, as measured by ion beam analysis (IBA). Difficulties on the incorporation of light hydrogen are related to the kinetic energy distribution of the impinging ions reaching the targets during the PLD growth process, ranging from 0.1 eV to 1000 eV [16]. The low energy population of the impinging species enhances layer-by-layer growth, and hampers the creation of trapping sites for the fuel particles. Within this incident energy range the formation of molecular ^{2}H$_2$ is also significant, reducing deuterium mobility and its interaction with the growing material. Additionally, at higher incident energies (~1 keV), the threshold energy for physical sputtering even promotes a preferential removal of the codeposited ^{2}H atoms [16]. The difficulties are not restricted to the PLD method. Recent experiments point the weak stability of codeposited W–^{2}H films produced by low energy magnetron sputtering techniques after exposure to atmospheric air. Trapped ^{2}H atoms are substituted by hydrogen atoms (^{1}H) diffused throughout the W matrix, leading to a fast isotope exchange effect [17,18].

In opposition to low energy deposition techniques, irradiation with energetic ion beams (within the keV range) has proven to be an efficient method to induce relevant lattice damage [19,20], enhancing the trapping of ^{2}H atoms in induced defects within the implantation depth zone. Most of ^{2}H becomes retained in monovacancies, and the retention in vacancy clusters induced by ion irradiation, involving higher trapping energies, highly occurs by increasing the impinging energy [19]. The depth profile of retained ^{2}H largely depends of the created clusters [19]. Nevertheless, even at room temperature, part of the hydrogen atoms is retained in interstitial lattice sites [19], and may diffuse towards the surface layers or deeply inside the W bulk far away from the implantation depth zone [19–21], while the enthalpies for hydrogen diffusion in W and in W–O based materials lie within the energy range of only 0.3–0.4 eV [21]. The consequence is that we may expect depth profiles for the retained ^{2}H slightly distinct of those predicted from the interaction of ^{2}H ions in W materials. The effect is advantageous aiming the use of the ion implantation technique with energetic ion beams to produce uniform-like depth contents of deuterium in W coatings.

Other deposition techniques than PLD are able to produce ^{2}H inclusions in the materials (^{2}H contents up to several at.%), without the ability to reproduce all the distinct microstructures. Moreover, it remains an issue in all the deposition techniques to reproduce detailed depth profiles ranging from uniform to implantation-like ones, as observed from the deposits in the walls of modern tokamaks. The authors point out that they can be reproduced by ion implantation.

The loading of light elements to reproduce W-based materials is also important to optimize techniques for elemental analysis. The main advantages of Laser Induced Breakdown Spectroscopy (LIBS) and Secondary Ion Mass Spectrometry (SIMS) techniques for the analysis of exposed PFC surfaces are that they provide a direct measurement of the elemental depth profiles throughout the entire deposited layers. Therefore, they are widely used to investigate codeposition mechanisms in tokamak walls [22–26]. Nevertheless, elemental quantifications using LIBS and SIMS are not standard free methods and calibration procedures need to be implemented involving standard free IBA techniques to directly provide elemental quantifications. Particularly, the best choice to calibrate them, enabling their use for a direct quantification of ^{2}H depth profiles in W deposits, requires the production of well-designed W–^{2}H proxies (standards; reference samples) with large amounts of deuterium. A logical solution for the effort is to produce W-based coatings by PLD and load them afterwards with desired contents of ^{2}H by ion implantation using energetic ^{2}H ion beams. The best practice for the calibration procedure demands that standards should present flat depth profiles of ^{2}H within the implanted depth zone, which may be implemented by using different ion implantation steps performed with ^{2}H$^+$ beams of distinct incident energies and fluences, aiming partial and optimized ion depth ranges along the target depths. Deviations to uniform ^{2}H depth profiles may be mitigated with the application of suitable partial fluences. It is also mitigated by a smooth diffusion of interstitial ^{2}H in the lattice matrix. The final depth profiles could be easily checked by observing the corresponding LIBS and SIMS isotopic yields of the removed material as a function of time. In a parallel way, ^{2}H amounts could be quantified with (standard free) IBA techniques such as Time-of-Flight Elastic Recoil Detection (ToF-ERDA) and Nuclear Reaction Analysis (NRA), providing a calibration procedure down to depth ranges of few hundreds of nanometers or of few micrometers, respectively.

SIMS is a well-established technique able to probe wide depth ranges with high elemental depth sensitivity and detection limits. A standard free quantitative elemental analysis provided by SIMS will be helpful in the future [27]. Even so, standards are easily used in SIMS calibration procedures with further analytical work. Most of all and due to radiation safety concerns, the focus is on the implementation of a standard free quantitative analysis by LIBS, while the optic technique is foreseen to be used in-situ to monitor the retention of radioactive tritium in the walls of experimental fusion reactors [22–24]. Deuterium loading acts as a proxy for the case of tritium addition. In a previous experiment, significant amounts of helium (He) were successfully incorporated in porous W (p-W) and compact W (c-W) coatings grown by PLD by ion implantation using energetic ^{4}He$^+$ ion beams. The irradiation procedure used a sequence of different incident beams performed at distinct incident energies and fluences (150 keV/2 × 10^{17} ion/cm^2, 100 keV/2 × 10^{17} ion/cm^2, 50 keV/1 × 10^{17} ion/cm^2) in order to assure uniform depth profiles of retained He along wide target depths [28]. The goal of the present work is to achieve similar results for the loading of ^{2}H by ion implantation following a similar procedure, this time with energetic ^{2}H$_2^+$ beams. The change of helium beams by deuterium ones implies a much lower irradiation damage imposed to the W materials (~6 times lower) [20]. In this sense, the proposed experiment is also a test to the loading procedure.

2. Materials and methods

Attempts to codeposit ^{2}H in W-based materials by PLD were performed, using the deposition procedure described in Section 2.1. Afterwards, and in order to explore the ion implantation route, different batches of W-based films were produced and irradiated with energetic ^{2}H ion beams to investigate the role of distinct compositions (W, W–O, W–O–N) and microstructures (columnar, porous) on the final depth profiles and retained amounts of deuterium.

2.1. Deuterium codeposition in W-based coatings

Light impurities are more easily retained in porous morphologies. Most of the attempts to codeposit ^{2}H by PLD were thus carried out with the growth of porous microstructures. Section 2.1 (see corresponding results in Section 3.1) briefly reports the production of porous W–O coatings by PLD using an argon-deuterium (Ar:^{2}H$_2$) mixture as background gas at distinct deposition pressures (30 Pa, 40 Pa, 60 Pa) with the aim to slightly modify the structure of the films, while preserving the porous nature (see Section 2.2.1). In a similar procedure aiming the growth of a porous W–O–N coating, an argon-nitrogen-deuterium (Ar:N$_2$:^{2}H$_2$) background atmosphere was used at a pressure of 50 Pa. Films with thicknesses of about ~1 μm were obtained. Characterization of the

achieved morphologies was carried out by Scanning Electron Microscopy (SEM) assisted by Energy Dispersive X-ray Spectroscopy (EDS). Elemental analysis was done by IBA, namely by using Elastic Backscattering Spectroscopy (EBS), NRA and ToF-ERDA techniques. Specific details of the PLD procedure and elemental analysis using incident ion beams are presented in Sections 2.2.1 and 2.2.3, respectively.

2.2. Deuterium loading by ion implantation

2.2.1. Production of W-based coatings for ion implantation experiments

The PLD apparatus used a pure target of W (99.99 % purity) as the tungsten source. W ablation was performed with focused Nd:YAG laser discharges of 532 nm at an energy fluence of 15 J/cm^2 per shot, with pulse time widths of 5–7 ns at a repetition rate of 10 Hz. Expanded plumes with the ablated material were directed towards Mo substrates maintained at room temperature and positioned at a target-to-substrate distance d_{TS} of 70 mm. In the vacuum regime, the ablated particle cloud expands free of collisions, and provides a directed spatial shock front with an increased plume length (I_P). Inert argon (Ar) or an argon-nitrogen (Ar:N$_2$) mixture were also used as background gas in the experimental chamber. By using a background atmosphere, the kinetic energy of the ablated particles is reduced during collisions with the gas by increasing its pressure, leading to a well-defined but diffused wave front with a lower plume length I_P compared to the vacuum regime. It is possible to tune the kinetic energy of the ablated material impinging the substrates by varying the deposition pressure, i.e., by controlling the ratio $L = d_{TS}/I_P$. In this way, the final microstructure and density of the produced films is selected [29]. Tuning $L \cong 1$, porous nanostructured films of lower density and lower adhesion to the substrates are deposited. The higher the pressure of the background gas, the lower the final density. Afterwards, oxidation of the porous films occurs under exposure to atmospheric air, being the gathering of O favoured with an enhanced porosity and effective surface area of the deposited materials [29]. More compact structures are formed with a ratio $L < 1$ [29]. Thin compact W films are commonly deposited on the substrates as interlayers, aiming at an improved adhesion of the coatings when porous structures are deposited. SEM-EDS measurements were carried out with a Zeiss Supra 40 field emission scanning electron microscope. Diffractograms were collected in the θ–2θ configuration with a Panalytical X'Pert PRO X-ray diffractometer assisted with a copper X-ray source. Table 1 presents additional deposition parameters used in the experiment, and the list of the four produced batches of coatings for the ion implantation campaign, from W1 to W4, each one of them containing four different samples. The growth of porous microstructures occurred at a deposition pressure of 50 Pa using pure Ar or a Ar-3%N mixture as background gas [30]. Compact morphologies were grown under vacuum (~10^{-2} Pa) [31]. Batches W1 and W2 were produced to investigate the role of slight changes in the composition and structure of porous W-based material (p-W) in the retained ^{2}H depth profiles. In the present example, the addition of N in the background gas imposed a partial replacement of the deposited O atoms (as in W1) by N atoms (W2). Also slight modifications in the porous microstructure at the nanoscale occurred (W2). W3 and W4 were used to compare the effect of distinct porous and compact structures, p-W and c-W, in the final ^{2}H profiles. Further details of the

PLD procedure can be found elsewhere [30,31]. The mass densities of the final p-W materials were checked by EDS [32] with an accuracy of 10 %. The accuracy of the measurements of the mass density in c-W materials was confirmed with the use of a quartz crystal microbalance (QCM) installed at the substrate holder and by X-ray Reflectometry (XRR) [32] with an accuracy of 1 %. Thicknesses for the deposited coatings slightly above 1 μm were assured by SEM for the implantation experiments.

2.2.2. Deuterium loading with sequential ion implantation steps

The ion implantation campaign was carried out at the Laboratory of Accelerators and Radiation Technologies (LATR) of IST using a high flux 210 kV Danfysik ion implanter, model S1090 [33]. A simple irradiation route of the W-based coatings was followed by using three distinct incident energies for the energetic ^{2}H$_2^+$ ion beams with a total fluence of 5×10^{17} ion/cm^2: 150 keV/2×10^{17} ion/cm^2, 100 keV/2×10^{17} ion/cm^2 and 50 keV/1×10^{17} ion/cm^2 [28] (75 keV, 50 keV and 25 keV by incident particle). The use of ^{2}H$_2^+$ molecular deuterium beams, instead of ^{2}H$^+$ beams, avoids an unexpected contamination of the targets during implantation by molecular hydrogen, ^{1}H$_2^+$. Current areal densities lower than 3 μA/cm^2 assured that the irradiation experiments with the metallic samples were performed at room temperature. At a steady impinging energy, the depth profile of the lattice defects induced by irradiation is coincident with the depth for the maximum nuclear energy deposition and is shifted towards the surface layer relative to the depth range of retained ions [34]. Therefore, and in order to counteract the effect of enhanced retained yields at pre-damaged depth layers, first, second and third irradiation steps were performed following a decrease of the incident ion energy [28]. The preparatory work assured that the implanted atoms became retained within the thickness of the coating (~1 μm). Depth profiles for the retained ^{2}H amounts and for the induced irradiation damage were evaluated with the SRIM code (SRIM-2008 update) [34]. Total amounts were obtained by summing the partial depth profiles calculated for each incident ion energy (75 keV, 50 keV or 25 keV per particle). The calculations took into consideration the partial ion fluences used for the implantation steps (2×10^{17} ion/cm^2, 2×10^{17} ion/cm^2 and 1×10^{17} ion/cm^2, respectively) and the measured mass density of the coatings (11.5 g/cm^3 for p-W, 19.2 g/cm^3 for c-W). Corresponding elemental stoichiometries and atomic densities were assumed in the SRIM calculations (see Section 3.2.2). A sequence of the entire implantation steps with predicted depth ranges for the incident ^{2}H particles are presented in Table 2 (Section 3.2.2). The individual damage dose induced by irradiation in the p-W and c-W targets was calculated using the "full damage cascades" option [35]. A displacement energy of 90 eV was selected for the W atoms, and lattice binding energies of 0 eV were used for all the three elemental components [36]. Default SRIM displacement energies of 28 eV and 10 eV were considered for O and H atoms, respectively [34]. Damage calculations took into consideration: the total events arising from primary deuterium knock-ons plus the collision cascades imposed by secondary atomic recoils after deuterium impact ("vacancy" file) [35,36], and the replacement collisions occurring when deuterium atoms fall into a vacancy left by a recoil target atom ("novac" file) [35]. Surface erosion caused by ion impact during the irradiation campaign was predicted using default SRIM values for

Table 1
Description of the background gas and produced coatings, with columnar W (c-W) and porous W (p-W) structures, including adhesion c-W interlayers.

Coating	Layer	Structure	Background gas	Background pressure (Pa)	Thickness[a] (μm)	Density (g/cm^3)	Adhesion layer
W1	1	p-WO	Ar (100 %)	50	>1.0	11.5	–
	2	c-W	vacuum	1.6×10^{-2}	~0.15	19.2	yes
W2	1	p-WON	Ar (97 %) + N (3 %)	50	>1.0	11.5	–
	2	c-W	vacuum	9×10^{-3}	~0.15	19.2	yes
W3	–	p-WO	Ar (100 %)	50	>1.0	11.5	–
W4	–	c-W	vacuum	9×10^{-3}	>1.0	19.2	–

[a] Nominal thickness.

Table 2

Implantation steps and ^{2}H ion depth ranges in c-W (W:O:H of 95:2:3; 19.2 g/cm^3) and p-W (W:O:H of 25:62:13; 11.5 g/cm^3); ion beams of molecular^2 H$_2^+$ were used.

Implantation step	Ion energy (keV)[a]	Ion fluence (ion/cm^2)	p-W		c-W	
			Rp (nm)	ΔRp (nm)	Rp (nm)	ΔRp (nm)
1	150 keV	2×10^{17}	396.0	114.0	332.1	121.2
2	100 keV	2×10^{17}	291.0	97.5	244.0	101.9
3	25 keV	1×10^{17}	168.1	67.9	141.4	69.0

[a] incident energies of molecular^2 H$_2^+$; half of the energy per single incident ^{2}H.

the elemental surface binding energies: 8.68 eV for W and 2 eV for both O and H atoms [34]. In a first ion implantation experiment, p-WO (W1) and p-WON (W2) porous batches were irradiated simultaneously. The density of the produced films is a dominant parameter having an effect on the ^{2}H depth profiles, and the behaviour was investigated by irradiating simultaneously the porous p-WO (W3) and the columnar c-W (W4) batches in a second ion implantation experiment. Both irradiations followed the same procedure, as described in Table 2.

2.2.3. Ion beam analysis

Before and after implantation, the coatings were analysed by EBS [37] using incident 1750 keV ^{1}H$^+$ ion beams, with the particle detector placed at a scattering angle of 165°. The incident energy is particularly useful to analyse the C and N contents of the coatings, taking advantage of the resonances of the ^{12}C(p, p$_0$)^{12}C and ^{14}N(p, p$_0$)^{14}N elastic scatterings of incident protons by ^{12}C and ^{14}N nuclei close to 1735 keV and 1741 keV, respectively [38]. As-implanted coatings were analysed simultaneously by NRA using the absorber foil method, and by Rutherford backscattering spectroscopy (RBS), using an incident 1000 keV ^{3}He$^+$ beams to quantify ^{2}H retained amounts in the irradiated surfaces by following the p$_0$ yield emitted from the ^{2}H(^{3}He, p$_0$)^{4}He nuclear reaction [37] at a reaction angle of 140°. Additional NRA and RBS spectra were collected using a 2300 keV ^{3}He$^+$ ion beam for the analysis of the W3 and W4 batches to better check the ^{2}H retained amounts in distinct microstructures. A 75 μm Mylar absorber foil was placed in front of the NRA detector to avoid the collection of ^{3}He particles backscattered from the analysed surfaces. RBS yields arising from the backscattering of ^{3}He$^+$ ions by W nuclei were used to normalise the NRA ones. All the experiments were performed using incident ion beams perpendicular to the analysed surfaces. Channel-to energy calibration of the NRA detection system was performed by analysing a pure Be plate and by resolving the p$_i$ yields emitted from the ^{9}Be(^{3}He, p$_i$)^{11}B nuclear reaction [39]. The EBS, NRA and RBS spectra collected from the individual samples were analysed simultaneously by using the NDF code [40].

Contrary to the limited depth resolution of the NRA analysis imposed by the used of the absorber foil method, ToF-ERDA is very sensitive to quantify the elemental composition of the samples within the surface layers [41]. Energy vs. time-of-flight 2D coincidence maps of the recoiled elemental species were collected using a 20 MeV ^{127}I^{6+} ion beam impinging the surface layers at an incident angle of 20° to the sample's surface. A gas ionisation detector [42] was located at a 37.5° forward direction with respect to the incident ^{127}I^{6+} beam. Elemental depth profiles of light isotopes and W were evaluated within a depth range down to 1×10^{18} at/cm^2. ToF-ERDA spectra were analysed using the POTKU code [43], enabling the analysis of possible elemental modifications imposed by the ^{127}I^{6+} irradiation, as elemental loss imposed by an erosion of light isotopic species. The procedure assured that the quantified light isotopic amounts were maintained during the analysis [43].

In view of the experimental detection geometries, kinematics and energy loss of ions in matter, the depth resolutions of IBA analyses are of the order of 10 nm for ToF-ERDA in flat surfaces and deteriorates very

fast with depth, 110 nm for EBS and it becomes optimized just to 250 nm for NRA due to the use of low energy 1000 keV ^{3}He ion beams [34,40,43].

Depth profiles for the retained ^{2}H and remaining elemental species were measured by SIMS along the entire depth of the as-implanted coatings with a double focusing magnetic sector instrument VG Ionex IX-70S. A focused 5 keV O$_2^+$ primary ion beam was used to sputter through the entire thickness of the films. Intensities of positive secondary sputtered ions at the particular mass-to-charge ratios were collected as a function of time. Additional details of the experimental procedure of the SIMS analysis are presented elsewhere [22,25,26].

3. Results and discussion

3.1. Deuterium codeposition in W-based coatings

SEM images with top views of the W films grown at Ar:^{2}H$_2$ background atmospheres at distinct deposition pressures (from 30 Pa to 60 Pa) are presented in Fig. 1a, b and 1c, respectively. Cauliflower-like morphologies are observed, revealing that the growing mechanism imposed the formation of porous structures. As predicted, related porosities raised by increasing the background pressure. The behaviour is also evidenced by the O levels in the surface layers, as revealed by EDS (see Fig. 1d) [29,30]. The corresponding EBS and ToF-ERDA quantifications for O are compatible with the EDS data. It is expected that enhanced porosity should favour the retention of ^{2}H in trap sites. Nevertheless, complementary NRA and ToF-ERDA results evidenced the low retained amounts of ^{2}H in all the films grown under Ar:^{2}H$_2$, but also under Ar:N$_2$:^{2}H$_2$ atmospheres. NRA measurements obtained with 1000 keV ^{3}He$^+$ ion beams reveal a lower atomic concentration of retained ^{2}H in the coatings of higher porosity. The quantified retained contents were close to ~0.25 at.%, ~0.20 at.% and ~0.13 at.% at the corresponding deposition pressures of 30 Pa, 40 Pa and 60 Pa of Ar:^{2}H$_2$. Similar atomic contents were obtained for the film grown in a Ar:N$_2$:^{2}H$_2$ mixture, (~0.18 at.%; 50 Pa). Corresponding deuterium contents at the surface layers were always lower than 0.1 at.% when quantified by ToF-ERDA. The experiment proved the ability of the PLD method to codeposit deuterium in W-based coatings. However, a new approach was necessary for an efficient deuterium loading.

3.2. Deuterium loading by ion implantation

3.2.1. Structural characterisation of W-based coatings

Fig. 2 shows SEM images of cross-sectional cuts of typical porous and columnar W structures grown by PLD. With the use of a diffused plasma plume tuned with a 50 Pa background gas, a columnar but irregular growth is obtained. At this base pressure, the main difference imposed by the use of a pure Ar or of an Ar-3%N mixture lies at the nanoscale with the formation of a homogeneous-like structure in presence of N (Fig. 2a vs. 2b). Top SEM image views of the same coatings also show the characteristic cauliflower-like growing mechanism (as observed in Fig. 1) [30], resulting the global morphology in a porous W (p-W) structure, leading to the gathering of significant amounts of O after the PLD deposition procedure under exposition to atmospheric air [29,30]. In a previous work, the presence of N was only identified when Ar-3%N were used during the PLD growth [30]. Porous microstructures grown under an Ar atmosphere (p-WO) and under Ar-3%N (p-WON) are presented in Fig. 2a and b, respectively. Coatings deposited under vacuum present the same columnar growth. Nevertheless, the columns have a more regular shape and a higher average height relative to those grown under a background gas. The top image views of the c-W coatings reveal a smooth surface and compact structure [30]. The smooth surface is also revealed in Fig. 2c, since the cross-section view was obtained with a slightly tilted geometry. SEM results are supported by X-ray diffraction analysis. A typical bcc W structure oriented along the (110) planes perpendicular to the surface of the coating is observed in all the
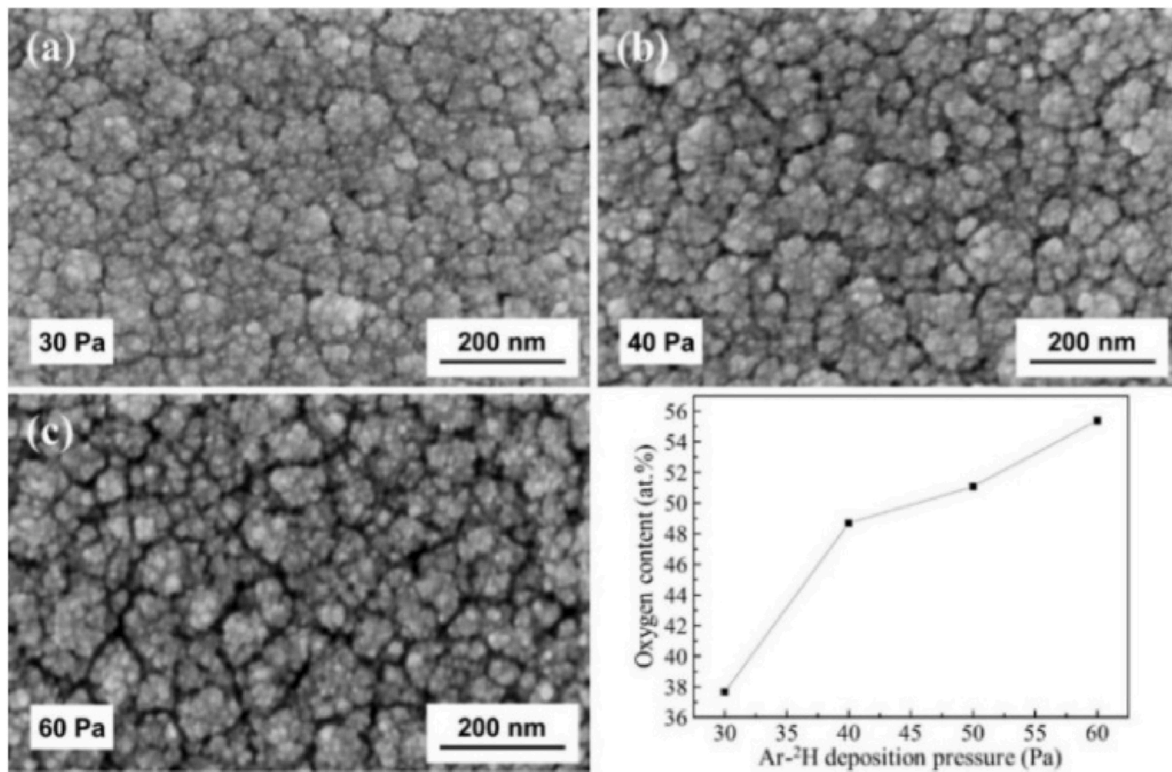
Fig. 1. Top views of W films deposited under Ar:^{2}H$_2$ background atmospheres: 30 Pa (a), 40 Pa (b) 60 Pa (c); corresponding oxygen contents measured by EDS (with additional data from the film grown under 50 Pa Ar:N$_2$:^{2}H$_2$ (d).
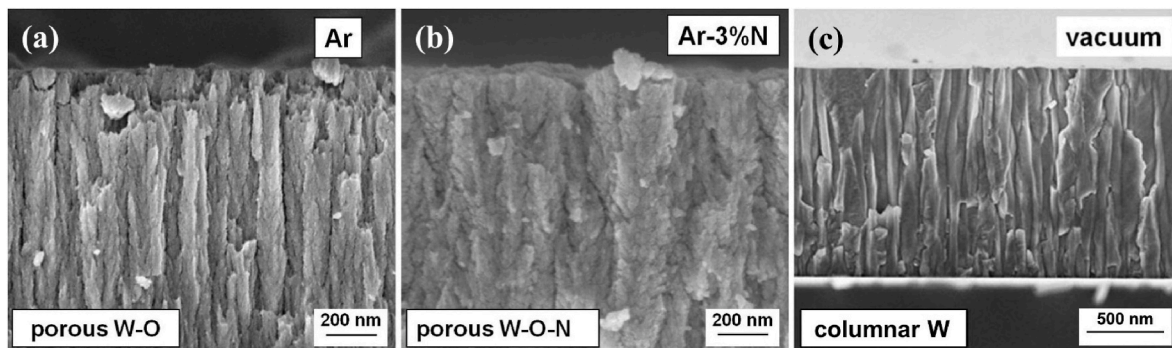

Fig. 2. SEM images of cross-section cuts of W-based coatings deposited by PLD exhibiting porous (p-W) and columnar (c-W) microstructures: porous W–O (p-WO) (a), porous W–O–N (p-WON) (b) and columnar W (c-W) (c), deposited under 50 Pa of Ar, 50 Pa of Ar-3%N, and under vacuum (~10^{-2} Pa), respectively.

diffractograms. The bcc grow is strongly oriented along this crystalline direction in the c-W coatings, whereas a significant broadening of the (110) reflection is observed from the p-W structures. By comparing the full width at half maximum of the reflections, and by using the Scherrer formula, crystallite domain sizes close to 16 nm and 7 nm were evaluated for the p-W and c-W structures, respectively [28,30,31].

Mass densities of 11.5 g/cm^3 and 19.2 g/cm^3 were calculated for the p-W and c-W coatings, respectively (see Table 1). Comparing with the mass density of a full bcc W microstructure (close to 19.3 g/cm^3) [31], practically no O and other impurities are predicted to be part of the c-W films. In opposition, significant amounts of O should be present in the p-W ones. In addition to the background atmosphere used during the PLD procedure, Table 1 shows the nominal thicknesses, mass densities and microstructures of the films deposited for the irradiation campaign (including the c-W adhesion interlayers grown between the porous films and Mo substrates).

3.2.2. Deuterium and irradiation damage depth profiles

The depth range of implanted deuterium depends on the energy loss imposed by the material to the incident ions, which in turn depends on elemental composition (Bragg's rule). Elemental depth profiles of W, O and N in the as-deposited coatings were measured by EBS. Additional ToF-ERDA analysis confirmed the main EBS results and the presence of a significant hydrogen (^{1}H) contamination achieved by exposure of the as-deposited materials to atmospheric air [30] (see Section 3.3). Aiming at the best comparison for the depth profiles of implanted ^{2}H between SRIM predictions [34] and IBA measurements, average W:O:H stoichiometries of 25:62:13 and 95:2:3 were chosen to characterize the p-W and c-W compositions of the as-deposited samples, respectively. They were used during the SRIM simulations (slight differences in the N and O elemental stopping powers were ignored). The stoichiometries and the measured volume densities of the as-deposited p-W and c-W films (11.5 g/cm^3, 19.2 g/cm^3) result in the corresponding atomic densities of 12.36×10^{22} at/cm3 and 6.61×10^{22} at/cm^3. These values were used to

calculate the partial atomic depth profiles of ^{2}H and induced irradiation damage after the first implantation step performed with the fluence of 2×10^{17} ion/cm^2 of 150 keV ^{2}H$_2^+$ ion beams (75 keV per incident particle). Elemental modifications imposed by deuterium loading after the first implantation steps were taken into consideration for the simulations related to the second implantation step. Simulations related to the third implantation step followed the same methodology. At the end, final depth profiles for the retained deuterium and irradiation damage were obtained with the sum of the partial contributions. Table 2 presents the simulated results for the average depth ranges (R_p) and related straggling ranges (ΔR_p) of incident ^{2}H$_2^+$ ions in both p-W and c-W materials. Lower depth ranges are expected for c-W due to its higher volume density and higher average Z-value and energy loss imposed to the incident particles [34]. Total and partial depth profiles after the first, second and third implantation steps for the retained deuterium amounts in both materials are shown in Fig. 3. The graph also shows the corresponding total depth profiles for the irradiation damage. The depth ranges of the induced defects are spread out shallower than those calculated for the retained ^{2}H. The behaviour may result in a deuterium uptake partially deviated towards the surface layers relative to SRIM predictions. Irradiation damage induced at higher incident ion energies enhances the trapping of ^{2}H atoms with further implantation steps. Wider depth ranges of retained atoms are also favoured by the retention of ^{2}H in interstitial sites [19], leading to a consequent diffusion along the W and W–O lattices [19–21].

Retention and irradiation damage calculations using the SRIM code are independent. They point to lower depth ranges and higher atomic fraction of retained ^{2}H in c-W. However, typical energies necessary to displace an atom from its lattice site (displacement energy) are much higher for the case of W than for O and H. Since c-W is almost composed of W, the predicted irradiation damage is much lower in c-W than in p-W. The retained fractions and induced damage calculated for both p-W and c-W structures reflect opposite behaviours. The measurement of the final deuterium amounts will express the role of damage effects in the retention mechanism.

The physical sputtering of W, O and H atoms is enhanced by decreasing the incident ion energies, while more cascade events will take place nearby the surface layer, promoting the escape of both impinging ions and lattice atoms. In opposition, incident energetic ions penetrate deeper into the bulk and become implanted. For the full implantation campaign, the calculated areal densities of sputtered atoms remained lower than 3.0×10^{15} at/cm^2 and 1.5×10^{15} at/cm^2 in both p-W and c-W coatings, respectively. Taking into account the atomic densities of p-W and of c-W, the predicted erosion depths are lower than 1 nm. The physical sputtering is negligible in the implantation campaign.

3.2.3. Ion beam elemental analysis

Fig. 4a presents EBS spectra collected from as-implanted W1 (p-WO) and W2 (p-WON) coatings and the corresponding fit lines obtained from the elemental analysis. Corresponding data from as-deposited W3 (p-WO) and W4 (c-W) are shown in Fig. 4b [40]. Vertical arrows indicate the energies corresponding to the presence of W, O and N in the surface layers (also C as surface impurity). W is the main elemental component in c-W and only a W surface backscattered yield is visible in the related spectrum (4b). In the case of the p-W structures, the W yield is widely reduced and EBS backscattered yields characteristic for O and N are identified, proving the presence of significant amounts of these elements
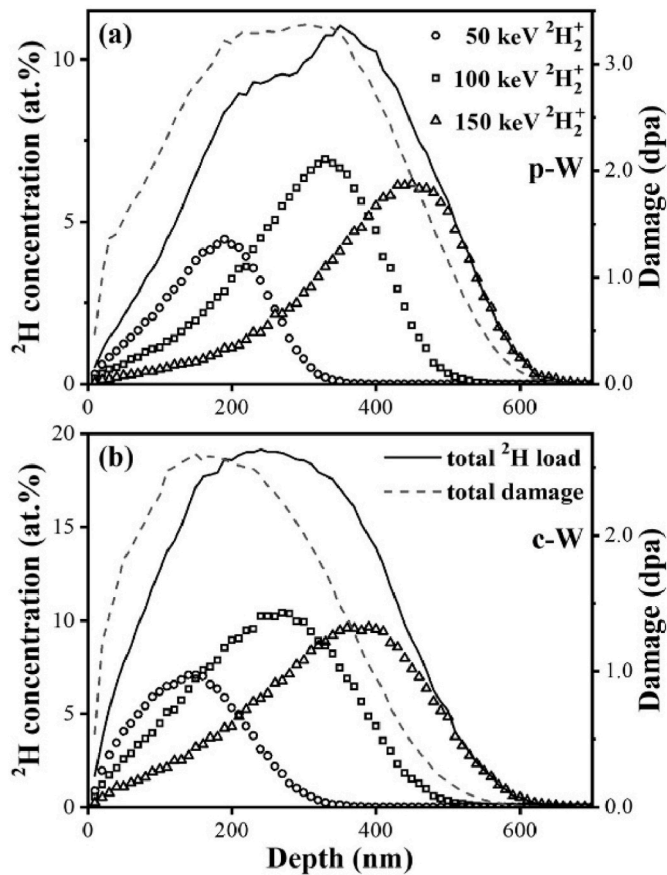

Fig. 3. Partial contributions of the ion implantation steps in the final depth profiles of ^{2}H retained amounts and irradiation damage as predicted by SRIM: (a) p-W; (b) c-W.
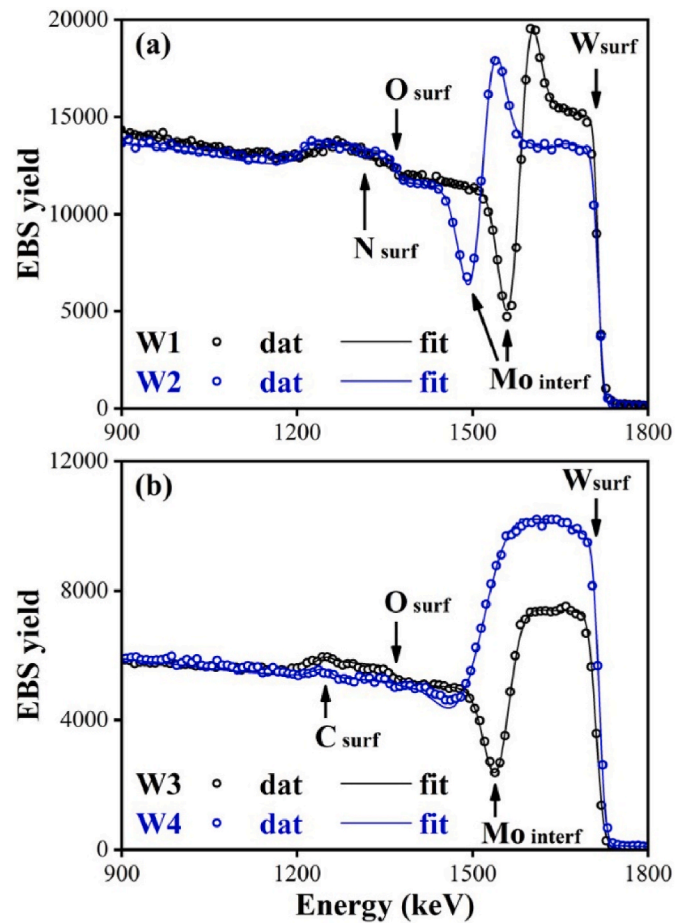

Fig. 4. EBS spectra collected with 1750 keV ^{1}H$^+$ ion beam from as-implanted coatings and fit lines achieved from the elemental analysis: porous W1 and W2 (a); porous W3 and columnar W4 (b).

in the films. The Mo substrate and the interface between the co-deposited layers and the substrate are also identified by EBS. The depth profiles of the W yields in the spectra collected from W1 and W2 also reveal the presence of thin and compact adhesion layers (c-W interlayers) at the interface between the porous coatings and the substrate (see Table 1). A more compact c-W structure in W4 enhances the spread of the energy of the incident ion beam (energy straggling). Therefore, the interface zone is more difficult to visualise in the EBS spectrum of W4. The analysis points to coating thicknesses slightly higher than 1 μm, as planned during the deposition procedure and confirmed by SEM. Before irradiation, the elemental compositions were quantified by EBS in order to prepare the implantation campaign.

Fig. 5 shows ToF-ERDA 2D coincidence maps (energy vs. time-of-flight) collected from as-implanted p-WO (W3) (5a) and c-W (W4) (5b) coatings, with elemental (isotopic) line signals clearly separated. The unidentified lines correspond to the $^{127}I^{6+}$ forward scattered from the irradiated surfaces, also collected in the spectra. The components visible in the TOF-ERDA spectra collected from as-irradiated porous W3 are ^{1}H, ^{2}H, C, O, W with lower amounts of N. Despite a surface C and O contamination, atmospheric components are not so visible in compact W4. ^{2}H retention is observed along the depth of the surface layers in both samples. The analysis of all the as-implanted porous structures reveals similar results. The main difference between them leads in the significant amount of N quantified in sample p-WON (W2).

Similar quantitative results were achieved from the analysis of the ^{2}H $(^{3}He, p_0)^{4}He$ yields in the NRA spectra collected from the as-implanted

p-WO and p-WON coatings (W1, W2 and W3), meaning that the incorporation of N in the porous structure did not change the main results. Contrary to that, the NRA yields observed from the as-implanted c-W coatings (W4) are significantly lower than those collected from the p-W ones. Fig. 6 compares the $^{2}H(^{3}He, p_0)^{4}He$ experimental NRA yields and corresponding fit lines achieved to quantify the retained ^{2}H contents [40] after the simultaneous implantation of the p-WO (W3; black colour) and c-W (W4; blue colour) coatings. Fig. 6 also includes data relative to the analyses performed with the incident 2300 keV (6a) and 1000 keV $^{3}He^{+}$ (6b) ion beams, aiming a simultaneous and complementary analysis at deeper depths as well as closer to the surface [40]. The enhanced NRA yields collected at 1000 keV $^{3}He^{+}$ (6b) are justified by the broad nuclear resonance of the $^{2}H(^{3}He, p_0)^{4}He$ reaction nearby 640 keV. ^{2}H contents retained nearby the coating's surface are quantified at the lower energy side of the NRA yield, while at backwards experimental geometries (as in the present case; reaction angle of 140°), the energy of the emitted p_0 protons increase by decreasing the energy of incident $^{3}He^{+}$ ions. The depth sensitivity of the NRA apparatus (energy resolution of ~180 keV) is not enough to evaluate slight changes in the retained ^{2}H contents nearby the surface layers and along the implantation depth zone. Nevertheless, the analysis points to fairly flat contents for the retained ^{2}H along depth ranges similar to those predicted by SRIM. The implantation depth zones for the retained ^{2}H amounts quantified by NRA and those predicted by SRIM (down to ~0.4–0.6 μm) are
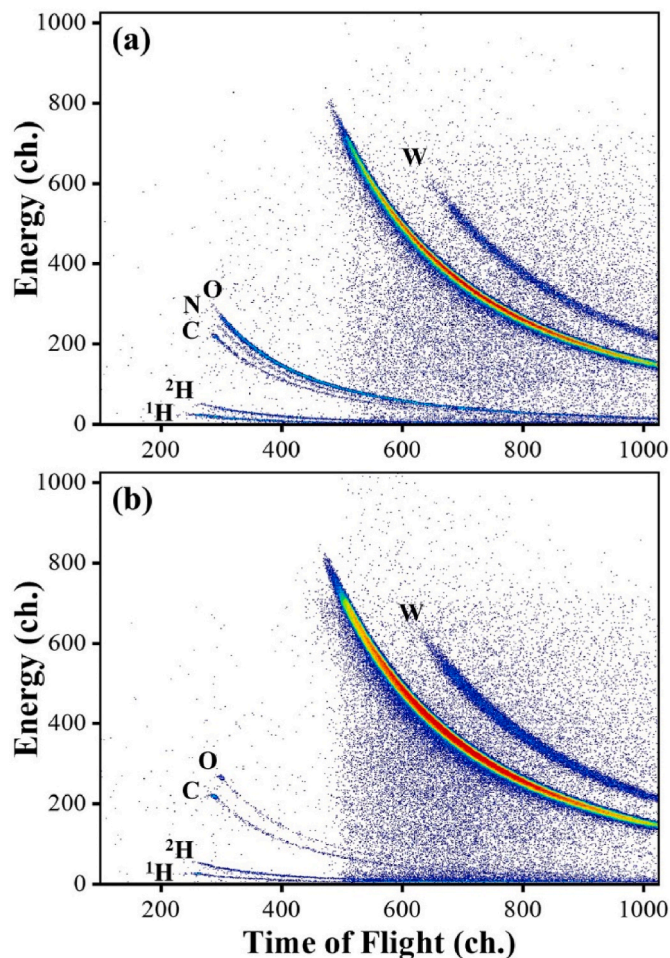

Fig. 5. ToF-ERDA 2D coincidence maps collected from as-implanted porous W3 (a) and columnar W4 (b) coatings, with elemental (isotopic) signals clearly separated. Axis units are given in channels.
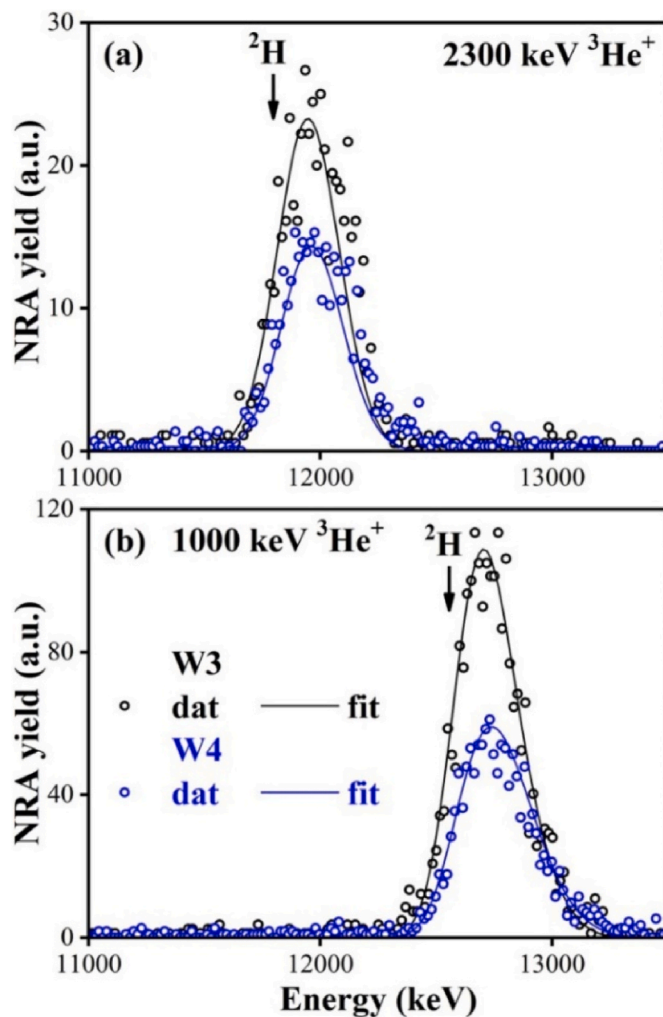

Fig. 6. NRA spectra collected with 2300 keV $^{3}He^{+}$ (a) and 1000 keV $^{3}He^{+}$ (b) ion beams and corresponding fit lines achieved from the elemental analysis to the as-implanted porous W3 and columnar W4 coatings.

compatible. At deeper depths, a steady decrease of the retained amounts nearby the limit of the implantation zone is quantified. The NRA yields point to lower retained ^{2}H amounts in c-W. Thinner depth zones are also quantified for c-W. Even so, similar full widths at half maximum (FWHM) are shown for the NRA yields of both p-WO (W3) and c-W (W4) films. The result is justified by the higher average atomic number (Z number) of compact tungsten, imposing a higher energy loss to the incident ^{3}He ions [34].

Fig. 7a and b shows the quantified depth contents obtained for the porous coatings W3: by ToF-ERDA nearby the surface layers within the depth range used for the elemental quantification (7a), and by the simultaneous EBS and NRA analysis down to deeper depths (7b). Aiming to compare these data with those achieved from columnar coatings, corresponding results obtained from the columnar coatings W4 are presented in Fig. 7c and d, respectively. Almost the quantified elemental yields agree with each other. The comparison between the SIMS yields relative to the ^{2}H amounts, normalized to the corresponding amounts quantified by NRA, and the corresponding NRA results, are also presented in Fig. 7b and d. The comparative data evidences that the depth profiles quantified by NRA where the deuterium content is maximum, and the broad edges with lower deuterium amounts, fairly follow those achieved by SIMS.

Table 3 present quantitative data of the entire elemental analysis. ToF-ERDA results are compared with those obtained by EBS and by NRA at similar depth ranges, close to the surface layers ($\sim 1 \times 10^{18}$ at./cm^2). Elemental EBS-NRA quantifications obtained for the entire implantation depth zone are also presented. Values for the depth ranges are also presented in metric units (nm), being the estimated data obtained from the mass densities of the W-based coatings (Table 1), from the elemental depth contents quantified by IBA (also presented in Table 3) and

corresponding atomic masses. Slight deviations between estimated and real thicknesses in metric units depend of the uncertainty in the measured mass densities and elemental composition of the films. The ^{1}H components present in the as-implanted films were only quantified by ToF-ERDA. EBS is only sensitive to quantify significant N contents, as those present in p-WON (W2) [38]. Taking advantage of the ToF-ERDA sensitivity for ^{1}H and N quantification and aiming the best comparison between the analytical results, these quantified values (by ToF-ERDA) were assumed as constant amounts and part of the elemental composition of the films along the entire coating's depth during the EBS and NRA quantifications. In Table 3, the concentrations obtained under this assumption are marked in parentheses. EBS and NRA analytical results assume an uncertainty of about 7.5 %, i.e., the uncertainty of the elemental stopping powers [34]. The TOF-ERDA analytical results have an uncertainty of about 6.0 % due to the elemental stopping powers plus the statistical uncertainty of the collected spectra.

A good agreement is observed from the overall comparison between ToF-ERDA and EBS-NRA analytical results, while similar compositions were measured along the depth of all p-W coatings. However, different ^{2}H, C and O amounts were measured at the surface of the c-W (W4) film. In this case, ToF-ERDA results relate to thin surface layers within a depth zone ranging from 200×10^{15} at/cm^2 to 500×10^{15} at/cm^2, and local deviations from an average elemental composition may occur. Due to the lower depth resolution of these techniques, EBS, NRA and even SIMS are not sensitive to analyse these elemental deviations in thin sublayers. A more compact c-W lattice is compatible with lower concentrations of ^{1}H, C and O impurities, as confirmed by ToF-ERDA. Higher C amounts were quantified in the c-W (W4) surface by EBS [38], as indicated with a vertical arrow in Fig. 4b. The nature of the deviation in the quantified O amounts in c-W is justified by the EBS analysis on the columnar
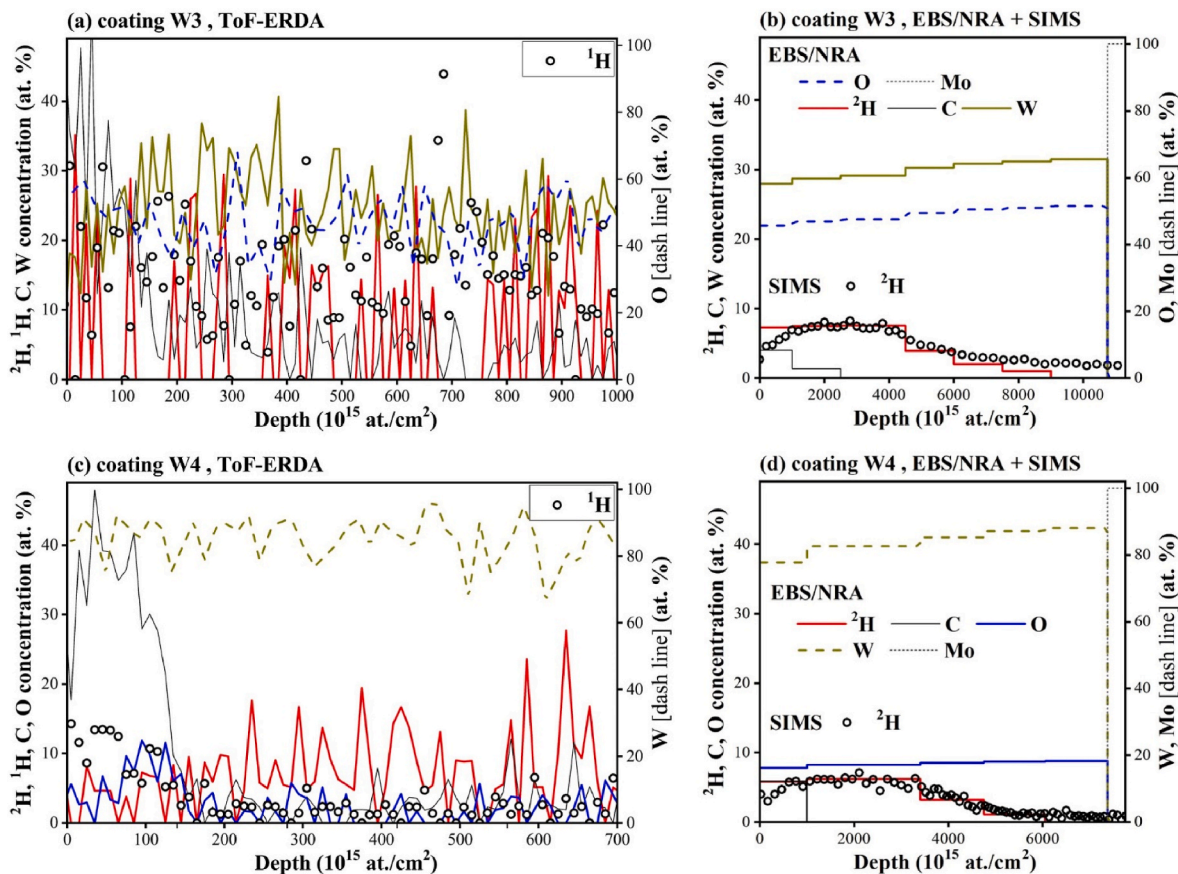

Fig. 7. Elemental depth profiles in porous W3 measured by: ToF-ERDA (a), and by EBS/NRA with a normalized ^{2}H yield achieved by SIMS (b); corresponding depth profiles measured from columnar W4 (c,d).

Table 3
Comparison of ToF-ERDA and EBS-NRA analytical results.

Sample	Depth range (10^{15} at/cm^2)	Depth range[a] (nm)	^{1}H (at. %)	^{2}H (at. %)	C (at. %)	N (at. %)	O (at. %)	W (at. %)	^{2}H (10^{15} at/cm^2)	Analysis
W1	0–1000	0–63	12.9	6.9	3.4	3.7	56	19.1		ToF-ERDA
W1	0–1000	0–76	(13)	7.7	–	(4)	52.6	24.0		EBS/NRA
W1	0–6000	0–457	(13)	7.7	–	(4)	52.6	24.0		EBS/NRA
W1	Total		–	–	–	–	–	–	4.6	NRA
W2	0–1000	0–66	13	6	1.9	27	33	20		ToF-ERDA
W2	0–1000	0–77	(13)	6.4	–	21.5	35.6	24.3		EBS/NRA
W2	0–7000	0–536	(13)	6.4	–	29.5	27.6	24.3		EBS/NRA
W2	Total		–	–	–	–	–	–	4.5	NRA
W3	700–1000	0–23	12.1	6	3.7	3.3	49	24		ToF-ERDA
W3	700–1000	0–26	(12)	7.3	4.0	(3)	45.7	28.0		EBS/NRA
W3	0–6000	0–528	(12)	7.0	1.1	(3)	47.2	28.8		EBS/NRA
W3	Total		–	–	–	–	–	–	4.4	NRA
W4	200–500	0–39	2.8	13	1.9	–	1.4	80		ToF-ERDA
W4	200–500	0–38	(3)	5.9	5.8	–	7.8	77.8		EBS/NRA
W4	0–4100	0–539	(3)	5.6	1.4	–	8.1	81.4		EBS/NRA
W4	Total		–	–	–	–	–	–	2.6	NRA

** inside parenthesis - ^{1}H and N contents used for the simultaneous EBS and NRA analysis.
[a] values estimated from local areal densities (10^{15} at/cm^2) and elemental composition, and mass densities (g/cm^3).

structure. In this case, the W yield was easily resolved during the analytical procedure by slightly decrease the W content, and by increasing the simulated O amount in W4, although an O yield is not visible in the EBS spectra (see the W4 spectra in Fig. 4b). A similar fit line could be obtained considering a higher amount of ^{1}H instead of O.

NRA analysis revealed similar implantation depth zones (6-7 × 10^{18} at/cm^2) and total retained ^{2}H amounts for all the p-W coatings (4.4–4.6 × 10^{17} at/cm^2), i.e., almost the total implanted fluences (5 × 10^{17} at/cm^2) became retained in the p-W targets. For the as-implanted c-W structure, the implantation depth zone and retained ^{2}H amounts are significantly lower (4 × 10^{18} at/cm^2 and 2.6 × 10^{17} at/cm^2). The results point to a lower retention behaviour in columnar c-W targets. A lower damage induced by ion irradiation and higher retained atomic contents of ^{2}H were predicted for the c-W films by SRIM (Fig. 3). Therefore, the quantified ^{2}H values, as quantified by NRA, highlight that the defects induced by irradiation impose a major role in the final retained amounts. By comparing the achieved results with data reported from real samples, we observed that the implanted ^{2}H amounts and final atomic contents (about 5–8 at.% of ^{2}H) are high enough to mimic the deposits recently found in tokamaks with full W first walls as in the ASDEX Upgrade [44, 45] and WEST [5,6] (where almost the ^{2}H contents are lower than ~2 at. %; lower than 5 at.% at WEST), evidencing the reliability of the method
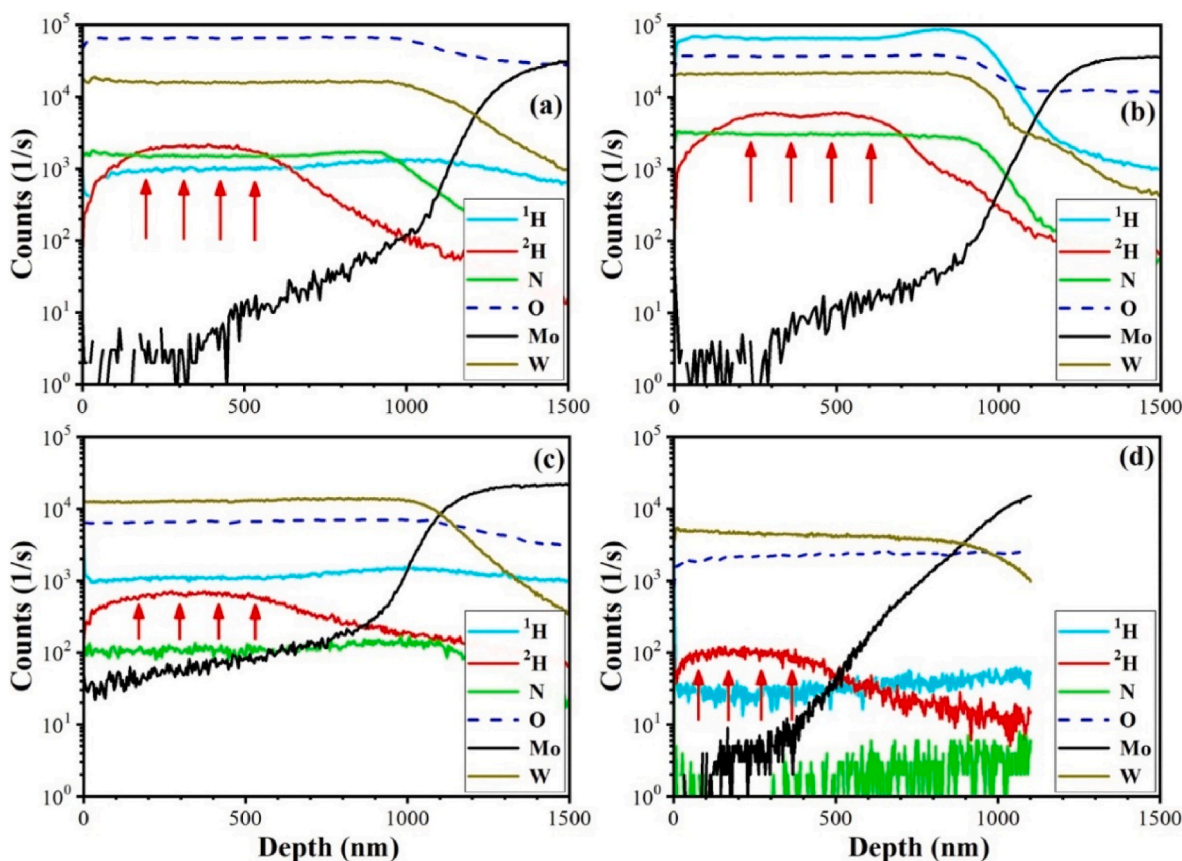

Fig. 8. SIMS depth profiles collected from the as-implanted porous coatings, W1 (a), W2 (b) and W3 (c), and columnar one, W4 (d). The vertical red arrows signalise the depth zone with the maximum ^{2}H contents.

to reproduce them.

Aiming at an optimized depth sensitivity, the elemental (isotopic) depth profiles of all the as-implanted coatings were achieved by SIMS. The results are shown in Fig. 8 using a vertical logarithmic scale to better visualise all the elemental yields. The measurements were performed with primary O ions, and it is impossible to precisely distinguish the part of the O signal arising from the real O contents in the samples. Therefore, the O yields are represented in Fig. 8 with dashed lines. The analyses of the as-implanted W1–W2 and W3–W4 samples were performed in distinct experiments. Even so, the depth profiles agree with the compositions quantified by ToF-ERDA, EBS and NRA. The presence of Mo nearby the surface is only apparent in porous W3 (Fig. 8c), while besides porous, the surface revealed to be very rough, and this also is the reason why ToF-ERDA quantifications for W3 were determined from slightly deeper layers (in the depth range from 700×10^{15} at/cm^2 to 1000×10^{15} at/cm^2; see Table 3). Regarding the particular profiles of implanted ^{2}H, we observe they present maximum uniform yields within the depth of the W-based films. The depth range where retained amounts exhibit their maxima (from 100-200 nm to 400–650 nm) are larger than the range of the implantation depth zones predicted by SRIM (Fig. 3), while significant amounts of ^{2}H are retained closer to the surface layers. Broad edged with lower retained amounts are also visualized nearby the surface layers and at deeper depths. The result also agrees with the depth profiles predicted for the total irradiation damage (Fig. 3). Highlighting the result, a balance involving the SRIM predictions for the total ^{2}H loading and irradiation damage depth profiles is compatible with the final ^{2}H depth ranges measured by SIMS (Fig. 3 vs. Fig. 8). Once again, lower depth ranges in the implantation depth zone are observed in compact c-W (W4). In contrast, higher amounts of N in porous p-WON (W2) decrease the energy loss imposed to the incident ions relative to porous p-WO (W1 and W3), evidencing the role of a slightly different porous composition in the retention mechanism. The maximum uniform yields collected for ^{2}H also point to the occurrence of a diffusion behaviour of interstitial deuterium along the W and W–O films [21], mitigating differences in the retained depth yields caused by ion implantation at distinct incident energies (Fig. 3). Therefore, deuterium still exists deeper inside the films, beyond the implantation depth zone [20], as visualized in the SIMS depth profiles. SRIM results point to lower amounts of retained ^{2}H at the surface layers. The behaviour predicts a reduced erosion of the surfaces by physical sputtering during irradiation with energetic beams, while the impinging ions are mainly implanted away from the surface layers.

SIMS analysis proves that the load of fairly constant deuterium amounts in W-based coatings grown by PLD can be obtained along a wide depth range following an ion implantation route using distinct energetic ion beams at optimized incident energies and fluences. ToF-ERDA and NRA results confirms the huge amounts of retained deuterium. These are the most relevant results of the present work, pointing the high efficiency of the ion implantation method to load deuterium in W-based materials.

4. Summary and conclusion remarks

The production of distinct W-based structures and compositions observed in the walls of modern tokamaks are able to be produced by PLD. Nevertheless, issues still exist on the PLD procedure for the codeposition of light deuterium. Solving these issues, the ion implantation technique using a sequence of implantation steps with energetic deuterium beams (of several keV) of distinct incident energies proved to be an efficient method to load the required deuterium amounts in as-deposited coatings. W-based coatings with typical porous (p-WO and p-WON) and columnar (c-W) microstructures were deposited on molybdenum plates by PLD. Afterwards, sequential ion implantation stages were performed following a decrease on the incident energy beam (150 keV, 100 keV and 50 keV ^{2}H$_2^+$ incident ions; total fluence of 5×10^{17} at/

cm^2). Maximum uniform deuterium contents of 5–8 at.% were obtained inside the p-W and c-W materials, with corresponding implantation depth zones in the range from ~100 to 200 nm down to ~400–600 nm. The total retained deuterium amounts were also significant: $(\sim 2.5-\sim 4.5 \times 10^{17}$ at/cm$^2)$. Lower atomic contents, depth ranges and retained deuterium amounts were achieved for c-W, in face of the higher density and heavier composition of this material. The achieved amounts are high enough to mimic almost the deuterium enriched p-WO, p-WON and c-W coatings present in the walls of modern tokamaks.

The comparison of the depth profile of deuterium, as measured by SIMS, with those simulated by SRIM for the induced irradiation damage and for the retained deuterium, enhances the role of the damage events in the retention mechanisms, while the measured depth profiles by SIMS are slightly deviated towards the surface layers, as the simulated irradiation damage. Part of the implanted deuterium becomes retained in trapping sites created during a previous implantation step. In the same way, a lower damage dose was predicted by SRIM in the c-W coating. Following the predicted damage dose, the quantified deuterium amounts in c-W are lower than in p-W. Nevertheless, SRIM predictions for the retained amounts point to an opposite behaviour (Fig. 3).

As observed in the SIMS profiles, the depth range of deuterium present flat and maximum contents along a wide depth range. Despite the use of different incident ion beam energies, the behaviour is enhanced by a deuterium diffusion along W and WO based materials, as signalized in previous published works. This is also signalized by SIMS with the smooth decrease of the deuterium yield beyond the coating's depth.

Implantation-like deuterium profiles are found in codeposited layers collected from the walls of present-day tokamaks. The possibility to mimic such layers by tuning the energy and fluence of energetic deuterium ion beams will be a major achievement in the future work. An additional goal of the project is the optimization of huge and uniform depth profiles of deuterium in W-based coatings aiming the calibration procedure of in-situ techniques as LIBS to monitor tritium inventory. PLD depositions followed by the presented ion implantation method, and elemental quantification assisted by IBA enables the success of the project.

CRediT authorship contribution statement

R. Mateus: Writing – original draft, Investigation, Formal analysis, Data curation, Conceptualization. **D. Dellasega:** Investigation, Formal analysis. **M. Passoni:** Investigation, Formal analysis. **Z. Siketić:** Investigation, Formal analysis. **I. Bogdanović Radović:** Investigation, Formal analysis. **J. Likonen:** Investigation, Formal analysis. **A. Hakola:** Investigation, Conceptualization. **E. Alves:** Investigation, Conceptualization.

Declaration of competing interest

The authors state no conflict of interest associated with the submitted work. All funding sources and institutional affiliations have been disclosed. The manuscript is original and not under consideration elsewhere.

Data availability

Data will be made available on request.

Acknowledgments

References

[1] R.W. Harrison, On the use of ion beams to emulate the neutron irradiation behaviour of tungsten, Vacuum 160 (2019) 355, https://doi.org/10.1016/j.vacuum.2018.11.050.

[2] A. Hakola, et al., Gross and net erosion balance of plasma-facing materials in full-W tokamaks, Nucl. Fusion 61 (2021) 116006, https://doi.org/10.1088/1741-4326/ac22d2.

[3] E. Fortuna-Zalema, et al., Post mortem analysis of a tungsten coated tile from the outer divertor strike point region of ASDEX upgrade, Nucl. Mater. Energy 9 (2016) 128, https://doi.org/10.1016/j.nme.2016.10.011.

[4] M. Rasinski, et al., High resolution scanning transmission electron microscopy (HR STEM) analysis of re-deposited layer on ASDEX Upgrade tile, Fusion Eng. Des. 86 (2011) 1753, https://doi.org/10.1016/j.fusengdes.2011.02.085.

[5] M. Balden, et al., Erosion and redeposition patterns on entire erosion marker tiles after exposure in the first operation phase of WEST, Phys. Scripta 96 (2021) 124020, https://doi.org/10.1088/1402-4896/ac2182.

[6] M. Diez, et al., Overview of plasma-tungsten surfaces interactions on the divertor test sector in WEST during the C3 and C4 campaigns, Nucl. Mater. Energy 34 (2023) 101399, https://doi.org/10.1016/j.nme.2023.101399.

[7] C. Ruset, et al., Development of W coatings for fusion applications, Fusion Eng. Des. 86 (2011) 1677, https://doi.org/10.1016/j.fusengdes.2011.04.031.

[8] M. Sala, et al., Exposures of bulk W and nanostructured W coatings to medium flux D plasmas, Nucl. Mater. Energy 24 (2020) 100779, https://doi.org/10.1016/j.nme.2020.100779.

[9] A. Uccello, et al., Effects of a nitrogen seeded plasma on nanostructured tungsten films having fusion-relevant features, Nucl. Mater. Energy 25 (2020) 100808, https://doi.org/10.1016/j.nme.2020.100808.

[10] M.H.J.'t Hoen, et al., Deuterium retention and surface modifications of nanocrystalline tungsten films exposed to high-flux plasma, J. Nucl. Mater. 463 (2015) 989, https://doi.org/10.1016/j.jnucmat.2014.11.025.

[11] O.V. Ogorodnikova, et al., Deuterium retention in dense and disordered nanostructured tungsten coatings, J. Nucl. Mater. 507 (2018) 226–240, https://doi.org/10.1016/j.jnucmat.2018.04.039.

[12] I. Jõgi, et al., LIBS study of ITER relevant tungsten–oxygen coatings exposed to deuterium plasma in Magnum-PSI, J. Nucl. Mater. 544 (2021) 152660, https://doi.org/10.1016/j.jnucmat.2020.152660.

[13] P. Paris, et al., In-situ LIBS and NRA deuterium retention study in porous W-O and compact W coatings loaded by Magnum-PSI, Fusion Eng. Des. 168 (2021) 112403, https://doi.org/10.1016/j.fusengdes.2021.112403.

[14] D. Dellasega, et al., Nanostructure formation and D retention in redeposited-like W exposed to linear plasmas, Nucl. Mater. Energy 36 (2023) 101492, https://doi.org/10.1016/j.nme.2023.101492.

[15] S. Markelj, et al., The effect of nanocrystalline microstructure on deuterium transport in displacement damaged tungsten, Nucl. Mater. Energy 37 (2023) 101509, https://doi.org/10.1016/j.nme.2023.101509.

[16] D.M. Zhang, et al., Influence of kinetic energy and substrate temperature on thin film growth in pulsed laser deposition, Surf. Coat. Technol. 200 (2006) 4027, https://doi.org/10.1016/j.surfcoat.2005.01.108.

[17] S. Krat, et al., Tungsten-deuterium co-deposition: experiment and analytical description, Vacuum 149 (2018) 23, https://doi.org/10.1016/j.vacuum.2017.12.004.

[18] S. Krat, et al., Effect of exposure of W-D co-deposited films to air on deuterium content in the films, Vacuum 219 (2024) 112764, https://doi.org/10.1016/j.vacuum.2023.112764.

[19] T. Ahlgren, et al., Simulation of irradiation induced deuterium trapping in tungsten, J. Nucl. Mater. 427 (2012) 152, https://doi.org/10.1016/j.jnucmat.2012.04.031.

[20] R. Mateus, et al., Deuterium and helium retention in W and W-Ta coatings irradiated with energetic ion beams, Nucl. Instrum. Methods Phys. Res. B 538 (2023) 41, https://doi.org/10.1016/j.nimb.2023.02.028.

[21] K. Kremer, T. Schwarz-Selinger, W. Jacob, Influence of thin tungsten oxide films on hydrogen isotope uptake and retention in tungsten - evidence for permeation

[22] J. Karhunen, et al., Applicability of LIBS for in situ monitoring of deposition and retention on the ITER-like wall of JET - comparison to SIMS, J. Nucl. Mater. 463 (2015) 931, https://doi.org/10.1016/j.jnucmat.2014.10.028.

[23] C. Li, et al., Review of LIBS application in nuclear fusion technology, Front. Physiol. 11 (6) (2016) 114214, https://doi.org/10.1007/s11467-016-0606-1.

[24] H.J. van der Meiden, et al., Monitoring of tritium and impurities in the first wall of fusion devices using a LIBS based diagnostic, Nucl. Fusion 61 (2021) 125001, https://doi.org/10.1088/1741-4326/ac31d6.

[25] J. Likonen, et al., Investigation of deuterium trapping and release in the JET ITER-like wall divertor using TDS and TMAP, Nucl. Mater. Energy 19 (2019) 166, https://doi.org/10.1016/j.nme.2019.02.031.

[26] A. Lahtinen, et al., Deuterium retention in the divertor tiles of JET ITER-Like wall, Nucl. Mater. Energy 12 (2017) 655, https://doi.org/10.1016/j.nme.2017.04.007.

[27] N.P. Barradas, J. Likonen, et al., Integration of SIMS into a general purpose IBA data analysis code, AIP Conf. Proc. 1336 (2011) 281, https://doi.org/10.1063/1.3586104.

[28] R. Mateus, et al., Helium load on W-O coatings grown by pulsed laser deposition, Surf. Coat. Technol. 355 (2018) 215, https://doi.org/10.1016/j.surfcoat.2018.02.089.

[29] A. Bailini, et al., Pulsed laser deposition of tungsten and tungsten oxide thin films with tailored structure at the nano- and mesoscale, Appl. Surf. Sci. 253 (2007) 8130, https://doi.org/10.1016/j.apsusc.2007.02.145.

[30] C. Pardanaux, et al., Post-mortem analysis of tungsten plasma facing components in tokamaks: Raman microscopy measurements on compact, porous oxide and nitride films and nanoparticles, Nucl. Fusion 60 (2020) 086004, https://doi.org/10.1088/1741-4326/ab9347.

[31] D. Dellasega, et al., Nanostructured and amorphous-like tungsten films grown by pulsed laser deposition, J. Appl. Phys. 112 (2012) 084328, https://doi.org/10.1063/1.4761842.

[32] A. Pazzaglia, et al., Reference-free evaluation of thin films mass thickness and composition through energy dispersive X-ray spectroscopy, Mater. Char. 153 (2019) 92, https://doi.org/10.1016/j.matchar.2019.04.030.

[33] E. Alves, et al., An insider view of the Portuguese ion beam laboratory, Eur. Phys. J. Plus 136 (2021) 684, https://doi.org/10.1140/epjp/s13360-021-01629-z.

[34] J.F. Ziegler, M.D. Ziegler, J.P. Biersack, Srim - the stopping and range of ions in matter (2010), Nucl. Instrum. Methods Phys. Res. B 268 (2010) 1818, https://doi.org/10.1016/j.nimb.2010.02.091.

[35] W.J. Weber, Y. Zhang, Predicting damage production in monoatomic and multi-elemental targets using stopping and range of ions in matter code: challenges and recommendations, Curr. Opin. Solid State Mater. Sci. 23 (2019) 100757, https://doi.org/10.1016/j.cossms.2019.06.001.

[36] T. Schwarz-Selinger, Deuterium retention in MeV self-implanted tungsten: influence of the damaging dose rate, Nucl. Mater. Energy 12 (2017) 683, https://doi.org/10.1016/j.nme.2017.02.003.

[37] M. Rubel, et al., Accelerator-based ion beam analysis of fusion reactor materials, Vacuum 78 (2005) 255, https://doi.org/10.1016/j.vacuum.2005.01.019.

[38] A.F. Gurbich, SigmaCalc recent development and present status of the evaluated cross-sections for IBA, Nucl. Instrum. Methods Phys. Res. B 371 (2016) 27, https://doi.org/10.1016/j.nimb.2015.09.035.

[39] N.P. Barradas, et al., Determination of the $^9Be(^3He,p_i)^{11}B$ (i = 0,1,2,3) cross section at 135° in the energy range 1-2.5 MeV, Nucl. Instrum. Methods Phys. Res. B 346 (2015) 21, https://doi.org/10.1016/j.nimb.2015.01.037.

[40] N.P. Barradas, C. Jeynes, Advanced physics and algorithms in the IBA DataFurnace, Nucl. Instrum. Methods Phys. Res. B 266 (2008) 1875, https://doi.org/10.1016/j.nimb.2007.10.044.

[41] P. Ström, et al., Characterisation of surface layers formed on plasma-facing components in controlled fusion devices: role of heavy ion elastic recoil detection, Vacuum 122 (2015) 260, https://doi.org/10.1016/j.vacuum.2015.04.019.

[42] Z. Siketić, N. Skukan, I. Bogdanović Radović, A gas ionisation detector in the axial (Bragg) geometry used for the Time-of-Flight Elastic Recoil Detection Analysis, Rev. Sci. Instrum. 86 (2015) 083301, https://doi.org/10.1063/1.4927605.

[43] K. Arstila, et al., Potku – new analysis software for heavy ion elastic recoil detection analysis, Nucl. Instrum. Methods Phys. Res. B 331 (2014) 34, https://doi.org/10.1016/j.nimb.2014.02.016.

[44] V. Rohde, et al., Dynamic and static deuterium inventory in ASDEX Upgrade with tungsten first wall, Nucl. Fusion 49 (2009) 085031, https://doi.org/10.1088/0029-5515/49/8/085031.

[45] K. Sugiyama, et al., Deuterium retention in tungsten used in ASDEX Upgrade: comparison of tokamak and laboratory studies, Phys. Scripta T159 (2014) 014043, https://doi.org/10.1088/0031-8949/2014/T159/014043.